A NEW APPROACH TO ANALYZING *HST* SPATIAL SCANS: THE TRANSMISSION SPECTRUM OF HD 209458 b

A. TSIARAS[1], I. P. WALDMANN[1], M. ROCCHETTO[1], R. VARLEY[1], G. MORELLO[1], M. DAMIANO[1,2], AND G. TINETTI[1]

[1] Department of Physics & Astronomy, University College London, Gower Street, WC1E6BT London, UK; angelos.tsiaras.14@ucl.ac.uk

[2] INAF—Osservatorio Astronomico di Palermo, Piazza del Parlamento 1, I-90134 Palermo, Italy

ABSTRACT

The Wide Field Camera 3 on the *Hubble Space Telescope* is currently one of the most widely used instruments for observing exoplanetary atmospheres, especially with the use of the spatial scanning technique. An increasing number of exoplanets have been studied using this technique as it enables the observation of bright targets without saturating the sensitive detectors. In this work, we present a new pipeline for analyzing the data obtained with the spatial scanning technique, starting from the raw data provided by the instrument. In addition to commonly used correction techniques, we take into account the geometric distortions of the instrument, the impact of which may become important when they are combined with the scanning process. Our approach can improve the photometric precision for existing data and also extend the limits of the spatial scanning technique, as it allows the analysis of even longer spatial scans. As an application of our method and pipeline, we present the results from a reanalysis of the spatially scanned transit spectrum of HD 209458 b. We calculate the transit depth per wavelength channel with an average relative uncertainty of 40 ppm. We interpret the final spectrum with $\mathcal{T}$-REx, our fully Bayesian spectral retrieval code, which confirms the presence of water vapor and clouds in the atmosphere of HD 209458 b. The narrow wavelength range limits our ability to disentangle the degeneracies between the fitted atmospheric parameters. Additional data over a broader spectral range are needed to address this issue.

Key words: methods: data analysis – methods: statistical – planets and satellites: atmospheres – planets and satellites: individual (HD 209458 b) – techniques: spectroscopic

1. INTRODUCTION

Transit light curves have proved to be an invaluable tool for determining the bulk and orbital parameters of exoplanets. In addition, observations of transits and eclipses at different wavelengths can reveal the thermal structure and composition of the atmosphere. In transmission spectroscopy, atmospheric opacities absorb/scatter small fractions of the stellar light passing through the planetary limb. This imprints a characteristic, wavelength-dependent variation on the mean transit depth, where the the ratio of the transmission spectra are 10–100 ppm to the radius of the star.

Atomic, ionic, molecular and condensate signatures from exoplanetary atmospheres have been identified both with ground-based and space-based instruments (e.g., Charbonneau et al. 2002; Vidal-Madjar et al. 2003; Redfield et al. 2008; Snellen et al. 2008, 2014; Swain et al. 2009a, 2009b, 2010; Linsky et al. 2010; Tinetti et al. 2010; Crouzet et al. 2012; Majeau et al. 2012; Waldmann et al. 2012, 2013; Todorov et al. 2013; Danielski et al. 2014; Sing et al. 2016).

A recent addition to the capabilities of *the Hubble Space Telescope* (*HST*) is the spatial scanning technique, which allows the sensitive infrared detector of Wide Field Camera 3 (WFC3) to observe bright targets. During a spatial scanning exposure, the instrument slews slowly along the cross-dispersion direction instead of staring at the target. As a result, the total number of photons collected is much larger, increasing the signal-to-noise ratio (S/N), without the risk of saturation. This observational strategy has already been successfully used to provide an increasing number of exoplanetary spectra (e.g., Deming et al. 2013; Crouzet et al. 2014; Fraine et al. 2014; Knutson et al. 2014a, 2014b; Kreidberg et al. 2014a, 2014b, 2015; McCullough et al. 2014; Stevenson et al. 2014; Line et al. 2016; Tsiaras et al. 2016).

The standard *HST* pipeline, CalWF3[3], and the spectroscopic package aXe[4] can reduce the *HST* staring-mode spectroscopic images and extract their respective 1D spectra. By contrast, scanning-mode spectroscopic images have a much more complicated structure, which can be described, to the zeroth-order approximation, as the superposition of many staring-mode images, each one slightly shifted along the vertical axis. Due to this structure, only an intermediate product of the CalWF3 package (IMA images) is valid when applied to scanning-mode data sets. In addition, the calibration/extraction routines included in the aXe package cannot be applied to spatially scanned spectra. In the literature, analyses of data sets obtained in scanning mode include custom routines to further reduce the IMA images and extract their calibrated 1D spectra.

In this work, we present a stand-alone, dedicated pipeline, able to produce 1D spectra from the raw scanning-mode spectroscopic images. In addition, because of geometrical distortions, the shifted staring-mode spectra, which construct each spatially scanned spectrum, are not identical to each other (Section 2.2), a behavior which was either partially or not taken into account in previous analyses. Our pipeline uses a new method to calibrate and extract the 1D spectra (Sections 2.3–2.5), eliminating possible issues caused by the scanning process. Adopting such an approach allows the efficient analysis of even longer scans, thus extending the capabilities of the spatial scanning technique.

As an application, we use our new pipeline to reanalyze the *HST*/WFC3 scanning-mode spectroscopic images of the transit of HD 209458 b (Deming et al. 2013). HD 209458 b is the very first transiting exoplanet detected (Charbonneau et al. 2000)

---

[3] http://www.stsci.edu/hst/wfc3/pipeline/wfc3_pipeline

[4] http://axe-info.stsci.edu/

Table 1
HD 209458 System Information

Stellar Parameters	
H (mag)[a]	6.591 ± 0.011
J (mag)[a]	6.366 ± 0.035
K (mag)[a]	6.308 ± 0.021
$T_{\rm eff}$ (K)[b]	6065 ± 50
[Fe/H] (dex)[b]	0.00 ± 0.05
M_* ($M_\odot$)[b]	1.119 ± 0.033
R_* ($R_\odot$)[b]	1.155 ± 0.016
$\log(g_*)$ (cgs)[b]	4.361 ± 0.008
Planetary Parameters	
$T_{\rm eq}$ (K)[b]	1449 ± 12
$M_{\rm p}$ ($M_{\rm Jup}$)[b]	0.685 ± 0.015
$R_{\rm p}$ ($R_{\rm Jup}$)[b]	1.359 ± 0.019
a (AU)[b]	0.04707 ± 0.00047
Transit Parameters	
T_0 (HJD)[c]	$2452826.628521 \pm 0.000087$
Period (days)[c]	$3.52474859 \pm 0.00000038$
Depth[b*]	0.014607 ± 0.000024
T_{14} (minute)[b*]	183.9 ± 1.1
b[b]	0.5070 ± 005
$R{\rm p}/R_*$[b]	0.12086 ± 0.00010
a/R_*[b]	8.76 ± 0.04
i (deg)[b]	86.71 ± 0.05

Notes.
[a] Cutri et al. (2003).
[b] Torres et al. (2008), ([b*] derived).
[c] Knutson et al. (2007).

and, consequently, the first studied with the transit (Charbonneau et al. 2002) and eclipse (Deming et al. 2005) spectroscopic methods. Its system parameters can be found in Table 1.

In terms of composition, transit measurements from space and ground have confirmed the presence of sodium in the atmosphere of HD 209458 b (Charbonneau et al. 2002; Sing et al. 2008; Snellen et al. 2008). Other UV observations suggested that the planetary atmosphere is in hydrodynamic escape (e.g., Vidal-Madjar et al. 2003; Holmström et al. 2008; Ben-Jaffel & Sona Hosseini 2010; Linsky et al. 2010). At longer wavelengths, where molecular signatures are stronger, water vapor has been identified by a number of measurements and teams (e.g., Barman 2007; Beaulieu et al. 2010; Deming et al. 2013). Carbon monoxide has also been detected (Snellen et al. 2010), while more carbon species, such as methane and carbon dioxide, have been suggested (Madhusudhan & Seager 2009; Swain et al. 2009a; Line et al. 2016). In addition, the thermal properties of the planet have been investigated by a number of teams (e.g., Burrows et al. 2007; Knutson et al. 2008; Griffith 2014; Line et al. 2014; Zellem et al. 2014; Evans et al. 2015; Schwarz et al. 2015).

In this paper, we use a range of different methods to detrend the extracted light curves from the instrumental systematics (Sections 3.1 and 3.2) and calculate the transit depth as a function of wavelength. The final spectrum is modeled using the fully Bayesian retrieval framework $\mathcal{T}$-REx described in Waldmann et al. (2015a, 2015b), based on the Tau code by Hollis et al. (2013), and using custom generated cross-sections based on the line lists from ExoMol (Yurchenko &

Tennyson 2014), HITRAN (Rothman et al. 2009, 2013) and HITEMP (Rothman et al. 2010) (Section 4).

2. DATA ANALYSIS

2.1. Observations—Raw Data Reduction

For our analysis, we downloaded the spatially scanned spectroscopic images of HD 209458 b (ID: 12181, PI: Drake Deming) from the MAST Archive.[5] More specifically, these images are the result of a single visit of the target (containing six *HST* orbits) using the infrared (IR) detector, the G141 grism and a scan rate of $0''.9\,{\rm s}^{-1}$. Each image consists of five nondestructive reads with a size of 266×266 pixels in the SPARS10 mode, resulting in a total exposure time of 22.32 s, a maximum signal level of $4.8 \times 10^4\,{\rm e}^-$ per pixel and a total scan length of about 170 pixels ($0''.121091$ per pixel). In addition, the data set contains, for calibration purposes, an undispersed (direct) image of the target with the F139M filter.

Our reduction process begins with the raw images, which have not been processed by the standard *HST* pipeline, CalWF3. For this reason, we have to apply the basic reduction steps explained in the *WFC3 Data Handbook* (Rajan et al. 2011, pp. 55–62) and the *WFC3 IR Grism Data Reduction Cookbook*[6] (pp. 16–17). These steps are listed below, and the corresponding CalWF3 routines are stated in brackets. Compared to CalWF3, we have modified only the routines which are not suitable for spatially scanned spectroscopic images and have also added the sky background subtraction.

Bias-level and zero-read corrections (ZSIGCORR—BLEV-CORR—ZOFFCORR). These initial steps are necessary due to the nature of the images, which consist of a number of nondestructive reads, also known as up-the-ramp samples. Our routine follows the implementation of CalWF3, beginning with calculating the zero-read flux (f_z). The WFC3 detector lacks a shutter and, as a result, the pixels collect photons before the exposure starts. The first nondestructive read of the detector is a reference for all the consecutive ones and it is referred to as the zero-read. f_z is the illumination recorded in the zero-read, and is important for the nonlinearity correction described later. It is calculated by subtracting from the zero-read the super-zero-read frame included in the *u1k1727mi_lin.fits* calibration file (Hilbert 2014), and stored in memory.

After the calculation of the zero-read flux, the value of reference pixels, located at the beginning and end of each row, are subtracted from each nondestructive read. The reference pixels are not sensitive to incoming light and subtracting them eliminates the $1/f$ noise between the nondestructive reads. Finally, the zero-read is subtracted from all the consecutive nondestructive reads, as it is the reference level.

Nonlinearity correction (NLINCORR). The IR detector of the WFC3 camera is known to perform nonlinearly with flux, following the equation:

$$F_{\rm c}(f) = (1 + c_1 + c_2 f + c_3 f^2 + c_4 f^3)f \qquad (1)$$

where F_c is the collected flux, f is the recorded flux, and c_n are the nonlinearity coefficients provided in the *u1k1727mi_lin.fits* calibration file.
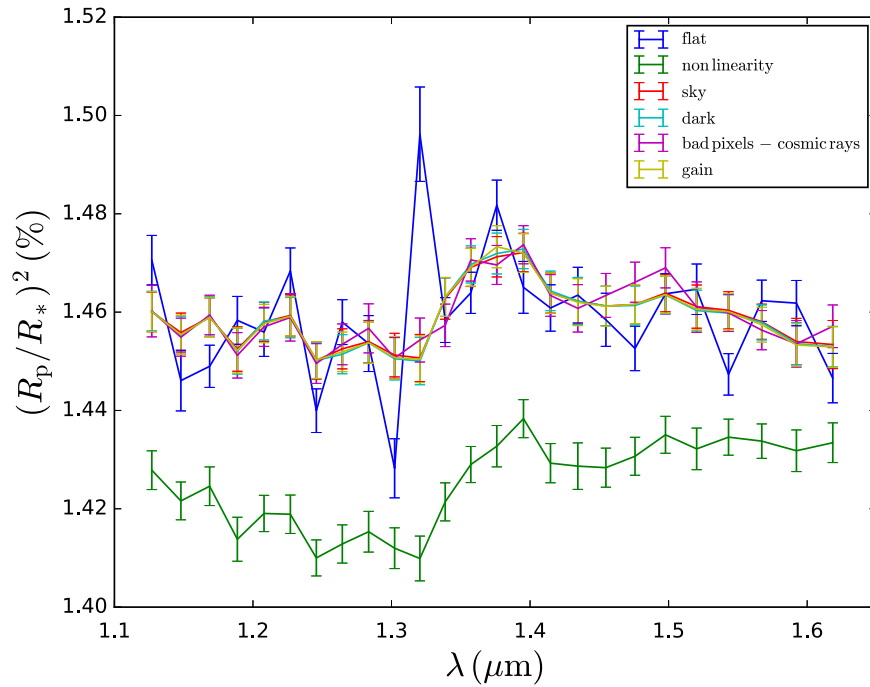
Figure 1. The HD 209458 b spectrum when switching off each reduction step, as indicated in the legend. For this data set, the reduction steps with the stronger effect are the flat-field (described in Section 2.4.3), the bad pixels/cosmic rays, and the nonlinearity corrections. The first two introduce strong scatter, while the third shifts and distorts the shape of the spectrum.

This correction is based on the absolute flux in a pixel, and not the difference from the zero-read. Hence, the zero-read flux has to be taken into account. In CalWF3, the amount of flux in the zero-read (f_z) is added to each nondestructive read (f_r) before the correction and subtracted after it, so that: $F_{\mathrm{final}} = F_c(f_r + f_z) - f_z$. In scanning-mode images, pixels with large zero-read fluxes are very common (very bright targets), and for those pixels F_{final} is overestimated. To avoid this additional flux, we also correct f_z before subtracting, so that: $F_{\mathrm{final}} = F_c(f_r + f_z) - F_c(f_z)$. For pixels where f_z is close to the saturation limit ($70,000\,\mathrm{e}^-$), the difference is of the order of $1000\,\mathrm{e}^-$.

Dark current subtraction (DARKCORR). The dark current in the WFC3/IR detector is nonlinear with time and also depends on the subarray mode and the sampling process. In agreement with CalWF3, we select from the provided super-dark files (Dulude et al. 2014) the one that matches with the data set and subtract the respective dark current frame from each non-destructive read.

Gain variations correction (FLATCORR). At this step, data number (DN) units are converted to electrons, in the same way as in CalWF3, while taking into account the gain variations between the four quadrants. Each nondestructive read is divided by the pixel flat-field frame included in the *u4m1335mi_pfl.fits* calibration file, and multiplied by the mean gain of the four amplifiers (mean gain = $2.35\,\mathrm{e}^-\mathrm{DN}^{-1}$).

Sky background subtraction. The sky background subtraction is not included in CalWF3. According to the *WFC3 IR Grism Data Reduction Cookbook* (pp. 16–17), the master-sky frame included in the *WFC3.IR.G141.sky.V1.0.fits* calibration file (Kümmel et al. 2011) has to be scaled and subtracted from the images prior to applying the wavelength-dependent flat-field (Section 2.4). This is a relative sky background template, which takes into account the variations of the sky background across the detector. The scaling factor is calculated from

dividing the least illuminated area of the image by the master-sky frame. For the case of HD 209458 b, we use an area on the left side of the spectrum. We avoid both the top and the bottom of the image due to the extended wings of the spectrum and a staring-like "ghost" spectrum, respectively. The latter is, possibly, the result of persistence from previous observations.

Bad pixels and cosmic rays correction (CRCORR). The final step in our reduction process is the correction of bad pixels and cosmic rays. Bad pixels have been identified during the calibration cycles and stored in the calibration file *y711520di_bpx.fits* (Hilbert 2012). In contrast, cosmic rays are randomly positioned on the detector and have to be identified in each image, independently. The cosmic rays detection and correction routine included in CalWF3 is based on the assumption that the flux in each pixel increases linearly with time. This behavior is expected for a static source, but not for a moving one and, consequently, the above assumption is not valid for scanning-mode data sets. To identify cosmic rays, we calculate two flags for each pixel; the difference from the average of the four horizontally neighboring pixels (*x*-flag) and the difference from the average of the four vertically neighboring pixels (*y*-flag). If a pixel's *x*-flag is 5σ larger than the other pixels in the column and its *y*-flag 5σ larger than the other pixels in the row, it is identified as a cosmic ray. In this way, we take into account the structure of the spatially scanned spectrum along both axes. We correct both the bad pixels (apart from the "blobs," which are not single pixels) and the cosmic rays by performing a 2D interpolation of the scientific image, excluding those pixels and then filling the gaps with the values of the interpolated function. We have to note here that, in CalWF3, the CRCORR step is applied before the FLATCORR step, but we choose to apply our routine at the end, to avoid propagating the interpolation uncertainties.

In our pipeline, there is the option of omitting any of the above reduction steps, and thus evaluating the effect of each
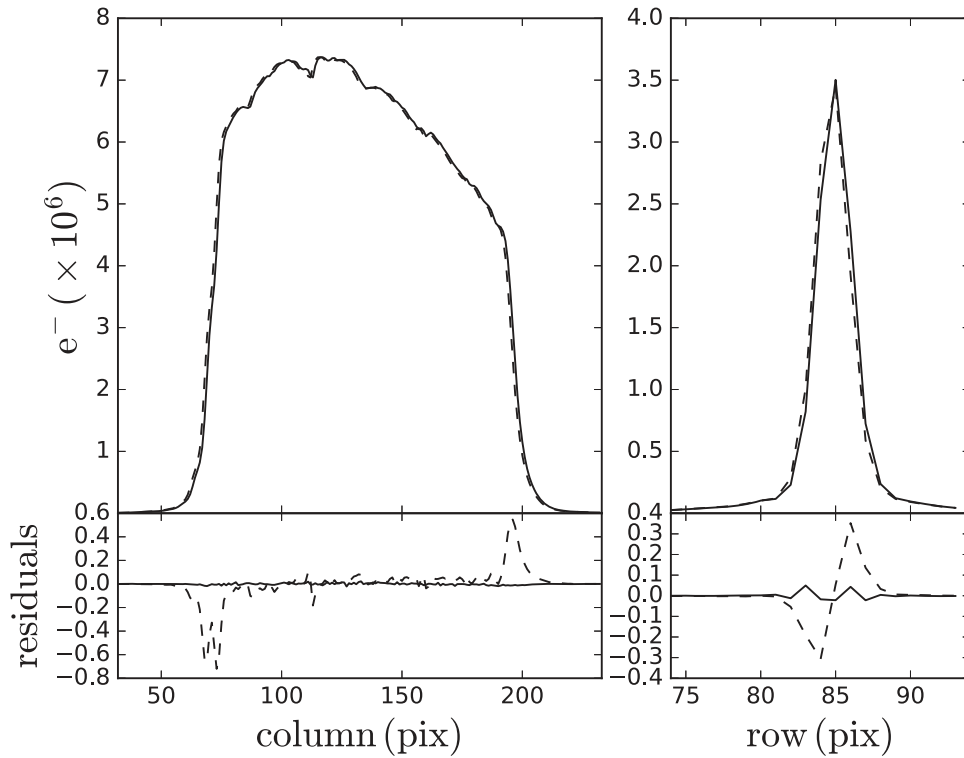
Figure 2. Left-top: normalized sum along the columns of the first (continuous) and the last (dashed, normalized) spatially scanned spectra of the visit. Left-bottom: difference between the two profiles before and after shifting, indicated by dashed and continuous lines, respectively. Right: same plots for the sum along the rows of the first nondestructive read.

one on the final spectrum. For HD 209458 b, we extracted the planetary spectrum (as described in the following sections) for cases where each reduction step is omitted, apart from the initial bias-level and zero-read corrections. Figure 1 shows the results, where we can see that the flat-field (described in Section 2.4.3), the bad pixels/cosmic rays, and the nonlinearity corrections have the stronger effect. However, these results are expected to vary between data sets, depending on the specific characteristics of each data set.

2.2. Structure of the Spatially Scanned Spectra and Extraction Challenges

A spatially scanned spectrum can be described as the superposition of many staring-mode spectra ("building blocks"), with each one slightly shifted along the vertical axis of the detector. The most common approach to produce 1D spectra from 2D spatially scanned ones, is to sum along the detector columns. However, the "building blocks" of a spatially scanned spectrum are neither identical to each other nor parallel to the detector rows, because:

1. there are significant dispersion variations along the vertical axis of the WFC3/IR detector (from about 4.47–4.78 nm/pix), caused by the 24 degree tilt about its horizontal axis,
2. the first-order spectrum of the G141 grism used, is inclined by 0.5 degrees with respect to the WFC3/IR detector rows,

as described in the *WFC3 Instrument Handbook* (Dressel 2012, pp. 173–174).

Because of the dispersion variations, the wavelength associated to a detector column is increasing toward its upper part. In the case of HD 209458 b (scan length of 170 pixels), for a column at 1.2 μm, the wavelength difference between the lower and the upper edge of the spatially scanned spectrum is 30 Å, while at 1.6 μm the difference is 70 Å. These values correspond to 0.6 and 1.5 pixels, respectively. As a result, 1D spectra resulting from summing along the columns of the detector vary by up to 1% between an intermediate scan of 60 pixels and the final scan of 170 pixels. For longer scans, such as 55 Cancri e (Tsiaras et al. 2016, 340 pixels), the effect is stronger and the discrepancy can be more than 2% (Section 2.5). An effort to correct for dispersion variations has been made by Kreidberg et al. (2014b) with a row-by-row interpolation, which rearranges the flux in each row to create a uniformly repeated spectrum along the scanning direction. Although this is a possible approach, it may restrict the achievable precision level, because the dispersion direction is inclined by 0°.5 and, therefore, the "building blocks" of the spatially scanning spectrum are not parallel to the detector rows.

Moreover, the inclined spectrum affects the wavelength calibration, as the wavelength solutions depend on the position of a pixel along the trace—i.e., the curve on which the spectrum lies—and not along the *x*-axis of the detector (see *aXe User Manual version 2.3*[7], pp. 76–77). The effect of summing along the columns in the wavelength calibration is evident in Wilkins et al. (2014), where the authors find an inconsistency between the extracted 1D stellar spectrum and the sensitivity curve of the G141 grism (Kuntschner et al. 2009). The empirical adjustment of the calibration coefficients, which these authors propose, is up to 10%.

---

[7] http://www.stsci.edu/institute/software_hardware/stsdas/axe/extract_calibrate/axe_manual
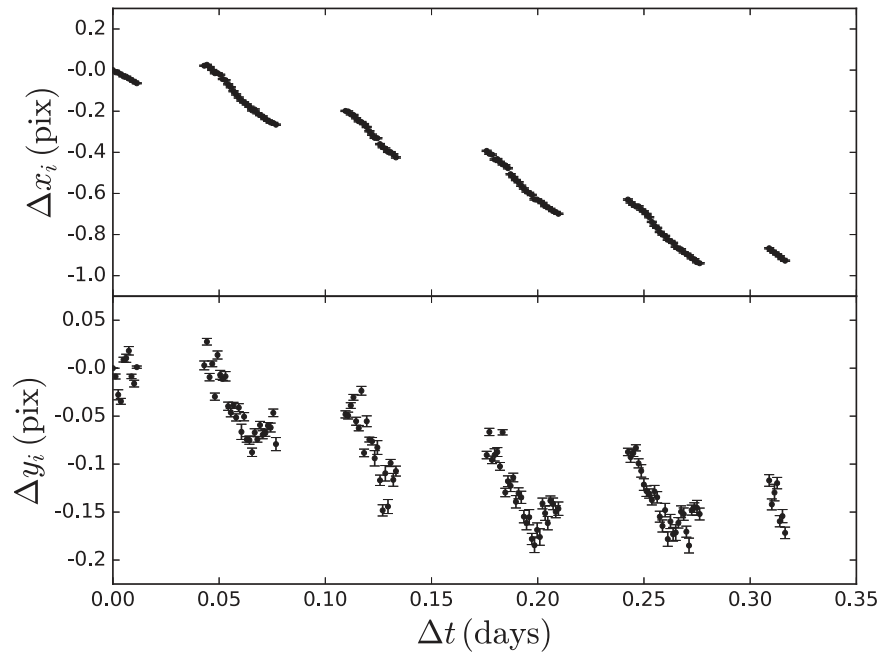
Figure 3. Horizontal (top) and vertical (bottom) shift for each image of the visit, relative to the first one.

To take into account the effects described above, we follow a calibration process (Sections 2.3 and 2.4), which monitors how the position of the dispersed photons changes during a scan, and define the wavelength-dependent photon trajectories (w.d. p.t.). We then use them to extract 1D spectra, which are both consistent with the structure of the spatially scanned spectra, and agree with the sensitivity curve of the G141 grism (Section 2.5).

2.3. Position Shifts

While the *HST* guiding system is stable, it fails to reset at exactly the same position as it was before a spatial scanning observation, causing horizontal position shifts of about one pixel over an entire visit (Deming et al. 2013; Fraine et al. 2014; Knutson et al. 2014b; Kreidberg et al. 2014b).

To calculate the horizontal shifts, we compare the structure of the first spatially scanned spectrum with all subsequent spectra, using the normalized sum along their columns (Figure 2, left), similar to Kreidberg et al. (2014b). For each consecutive image, i, we interpolate and fit for the horizontal shift, Δx_i, relative to the first one. Note here that the sums used above are corrected for the static (non-wavelength-dependent) component of the flat-field, to avoid the bias introduced by its structure. The final values will be used in the following section to define the wavelength-dependent photon trajectories (w.d.p. t.), and ,therefore, the left and right edges of the extraction apertures.

Horizontal shifts are important as they displace the spectrum on the detector and also introduce additional systematics to the spectral light curves, such as undersampling (Deming et al. 2013; Wilkins et al. 2014). For this particular data set, we find horizontal shifts of about 0.9 pixels over the visit (top panel in Figure 3). If not taken into account, such shifts introduce variations of up to 250 ppm in the planetary spectrum.

In addition, shifts of the vertical position from which the scan starts (Δy_i) are calculated from the first nondestructive read of each exposure. We apply the same method as for the horizontal shifts described above, with the difference that here we sum along the rows instead of the columns (Figure 2, right). Finally, we calculate the scan length (l_i) by fitting an extended Gaussian function on the sum along the rows of the last nondestructive read. The results will be used later to define the upper and lower edges of the extraction apertures. For this observation, both vertical shifts (0.2 pixels over the visit, bottom panel in Figure 3) and length variations ($l_i = 164.688 \pm 0.017$ pixels over the visit) are not significant enough to affect the final planetary spectrum.

2.4. Wavelength Calibration

2.4.1. Position of the Star

The key information for calibrating a WFC3/G141 spectrum is the physical position of the star (x^*, y^*) on the full detector array (Kuntschner et al. 2009). For this purpose, every spectrum should be accompanied by an undispersed (direct) image of the star, taken with the filter F140W. In the case of spatially scanned spectra, the vertical position (y^*) is not constant and so it cannot be determined from the direct image. In contrast, the horizontal position (x^*) is given by the equation:

$$x^* = x_0 + (507 - 0.5L) + \Delta x_{\mathrm{off}} + \Delta x_{\mathrm{ref}} \qquad (2)$$

where x_0 is the result of fitting a 2D Gaussian function to the direct image, L is the size of the direct image array, 507–$0.5\,L$ is the difference between the coordinate systems of the subarray used for the direct image and the full detector array (this correction gives the absolute position on the detector, and the number 507 is used, because the calibration coefficients do not take into account the reference pixels), Δx_{off} is the difference in the centroid offsets along the x-axis between the filter used for the direct image and the filter F140W, and Δx_{ref} is the difference in the chip reference pixels between the WFC3 aperture used for the direct image and the WFC3 aperture used for the dispersed image. Details and tables of values for each of
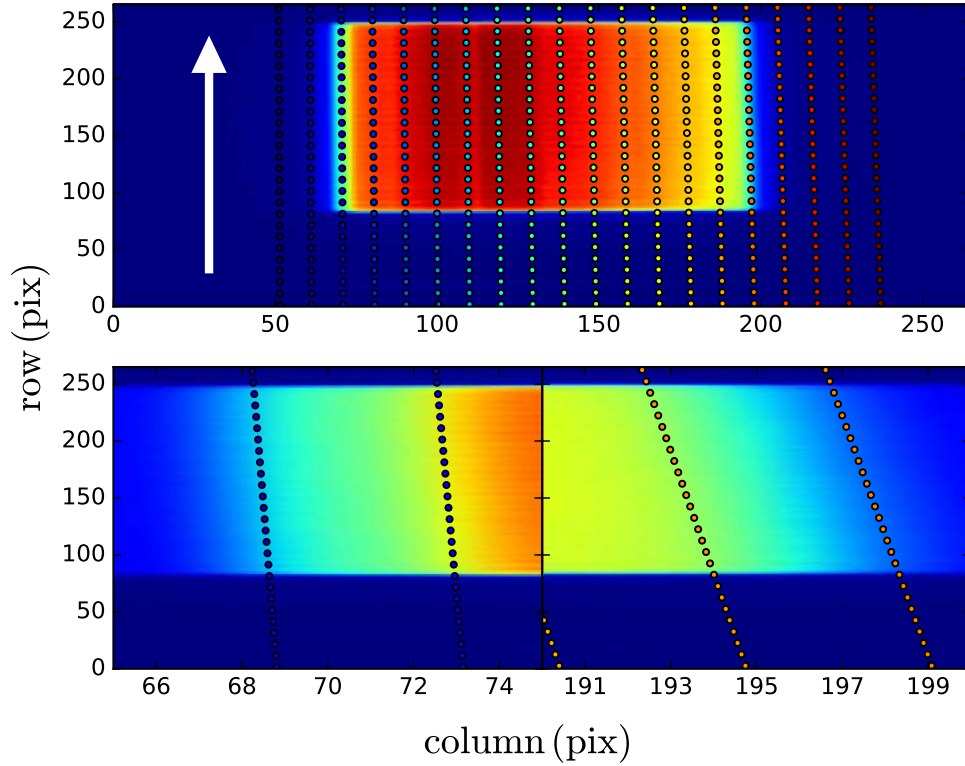
Figure 4. Top: position of the dispersed photons with different wavelengths (colored points) as the star moves along its scanning trajectory (white arrow). Bottom: left and right edges of the spectrum, where we can appreciate how accurately the grid follows the data.

the above correction parameters can be found in Appendix A. For HD 209458 b, these values are (in pixels): $x_0 = 137.5$ (for the first scan), $L = 256$ (subarray used: SQ256SUB), $\Delta x_{\mathrm{off}} = 0.027$ (filter used: F139M), $\Delta x_{\mathrm{ref}} = -107$ (WFC3 apertures used: direct image: IRSUB256, spatial scans: GRISM256)

The limited observational time in each *HST* visit allows the observers to include only one undispersed image, at the beginning of each visit. With this image, we can calculate the x^*, which corresponds to the first scan (x_1^*), but, for any subsequent scan, we have to use the horizontal shifts calculated in the previous section:

$$x_i^* = x_1^* + \Delta x_i \tag{3}$$

2.4.2. Calculating the Wavelength-dependent Photon Trajectories (w. d.p.t.)

As described in the *aXe User Manual version 2.3* (pp. 76-77), the trace of a staring-mode spectrum on the detector is:

$$y - y^* = a_t(x - x^*) + b_t \tag{4}$$

where

$$\underbrace{a_t}_{\text{or DYDX\_A\_1}} = \begin{cases} a_{t0} + a_{t1}x^* + a_{t2}y^* + \\ a_{t3}x^{*2} + a_{t4}x^*y^* + a_{t5}y^{*2} \end{cases}$$

$$\underbrace{b_t}_{\text{or DYDX\_A\_0}} = b_{t0} + b_{t1}x^* + b_{t2}y^*$$

and the wavelength solution is:

$$\lambda = a_w d + b_w \tag{5}$$

where

$$\underbrace{a_w}_{\text{or DLDP\_A\_1}} = \begin{cases} a_{w0} + a_{w1}x^* + a_{w2}y^* + \\ a_{w3}x^{*2} + a_{w4}x^*y^* + a_{w5}y^{*2} \end{cases}$$

$$\underbrace{b_w}_{\text{or DLDP\_A\_0}} = b_{w0} + b_{w1}x^* + b_{w2}y^*$$

and (x^*, y^*) is the physical position of the star on the full detector array, d is the distance from the source along the trace and $(a_{tn}, b_{tn}, a_{wn}, b_{wn})$ are the *HST* calibration coefficients included in the configuration file *WFC3.IR.G141.V2.5.conf* (Kuntschner et al. 2009, Appendix B).

In the case of spatially scanned spectra, the star is moving on the detector. We track the changes in the positions of the dispersed photons during each scan and define the w.d.p.t. by following these steps:

1. work out the position of the dispersed photons on the main trace (x_λ, y_λ) as function of y^* and wavelength (λ), using Equations (4) and (5) (for the proof of the following equations see Appendix B):

$$x_\lambda = x^* - \frac{a_t b_t}{1 + a_t^2} + \frac{\lambda - b_w}{a_w}\cos[\tan^{-1}(a_t)]$$

$$y_\lambda = a_t(x_\lambda - x^*) + b_t + y^* \tag{6}$$

2. assume x^* to be constant during a scan, but different from one scan to another (x_i^* from Equation (3)),
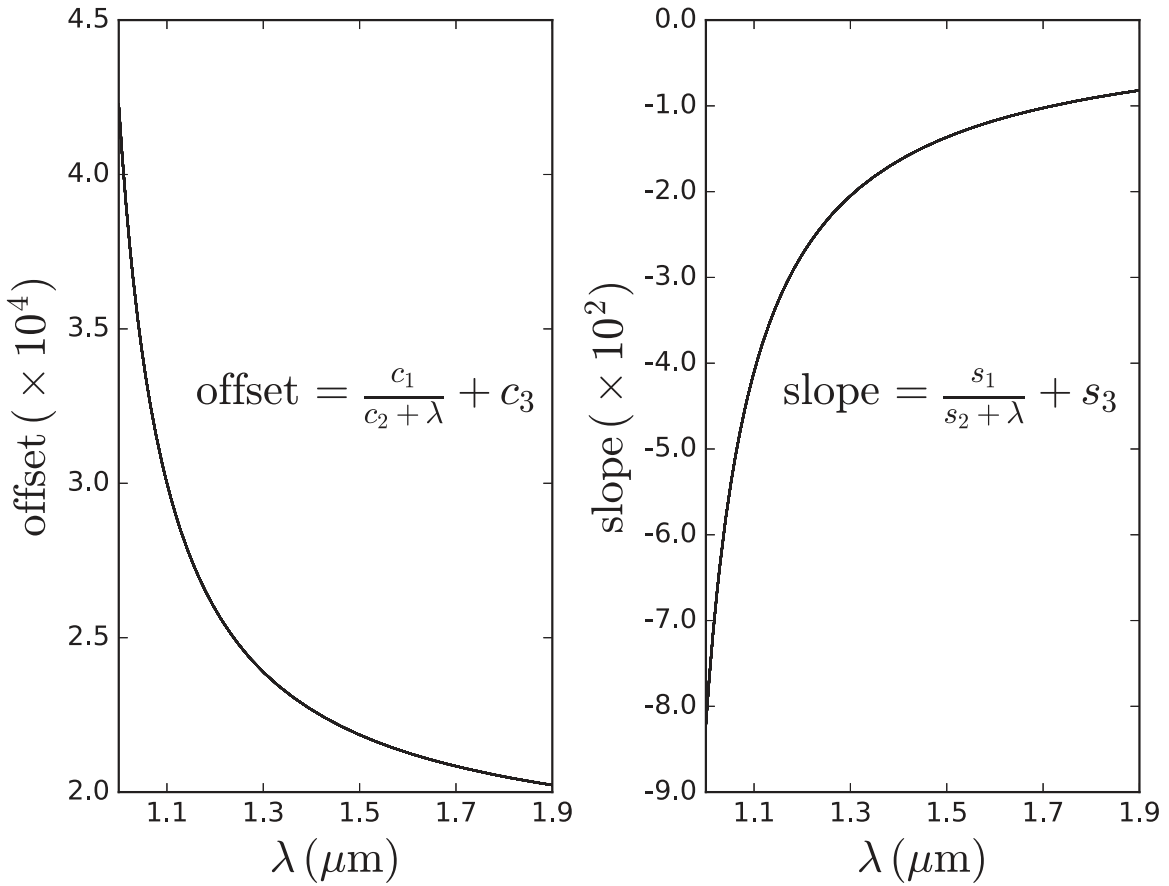3. let y^* vary uniformly across the length of the subarray, corresponding to the vertical scan,

6

Figure 5. The offset and slope of the w.d.p.t. as functions of wavelength.

4. let λ vary uniformly from 1–1.8 Å, covering the whole response range of the G141 grism,
5. from all the (y^*, λ) pairs, use Equation (6) to create a large grid of $(\lambda, x_\lambda, y_\lambda)$ points (Figure 4),
6. fit on the grid points the function of the w.d.p.t.:

$$y_\lambda = \left(\frac{c_1}{c_2 + \lambda} + c_3\right) + \left(\frac{s_1}{s_2 + \lambda} + s_3\right)x_\lambda. \quad (7)$$

For a given wavelength, Equation (7) represents a straight line across the detector, the line on which the photons of this particular wavelength move during the scan. In Figure 5, the offset and slope of these lines are plotted as functions of wavelength.

2.4.3. Wavelength-dependent Flat-field

We also use the wavelength grid created in the previous section to apply the wavelength-dependent flat-field, as described in the *aXe User Manual version 2.3*. We can find the wavelength as a function of position by fitting a different 2D function on the grid points:

$$\lambda = \kappa_0 + \kappa_1 x_\lambda + \kappa_2 y_\lambda + \kappa_3 x_\lambda^2 + \kappa_4 x_\lambda y_\lambda + \kappa_5 y_\lambda^2. \quad (8)$$

The wavelength-dependent flat-field for each pixel (x, y), is then:

$$F(x, y) = \sum_{i=0}^{i=3} F_i(x, y)\left(\frac{\lambda(x, y) - \lambda_{min}}{\lambda_{max} - \lambda_{min}}\right)^i \quad (9)$$

where F_i are the different extension arrays and λ_{min}, λ_{max}, the wavelength coefficients provided in the flat-field cube *WFC3.IR.G141.flat.2.fits* (Kuntschner et al. 2011).

2.5. Extraction of 1D Spectra

The 1D spectra are extracted from apertures of quadrangular shape, specifically calculated for each wavelength bin $(\lambda_1 - \lambda_2)$ per frame (Figure 6). The left and right edges of each quadrilateral are given by the w.d.p.t. (Equation (7)) for $\lambda = \lambda_1$ and $\lambda = \lambda_2$, respectively. The upper and lower edges are given by the spectrum trace (Equation (4)) for $y^* = y_1 + \Delta y_i$ and $y^* = y_1 + \Delta y_i + l_i + y_2$, respectively. Δy_i is the vertical position shift and l_i is the scan length of each spatially scanned spectrum, as calculated in Section 2.3. The values for y_1 and y_2 are chosen in order to correspond to 15 pixels below and 7 pixels above the spatially scanned spectrum (for this data set $y_1 = 442.5$ and $y_2 = 7$ pixels).

An issue concerning the extraction method, is that we have to take into account fractional pixels at the edges of the photometric apertures. As a first approximation, we used the fraction of the pixel area inside the extraction aperture. While testing this method, we concluded that this approach intensifies the wavelength-dependent systematics, which are caused by the horizontal shifts and the low spectral resolution of the spectrum (Section 3.2). A better approach for those pixels is a second-order 2D polynomial distribution of the flux. The coefficients of this 2D function are calculated analytically, so that its integral inside the pixel of interest and inside each surrounding pixel, are equal to their flux levels. We can then calculate the
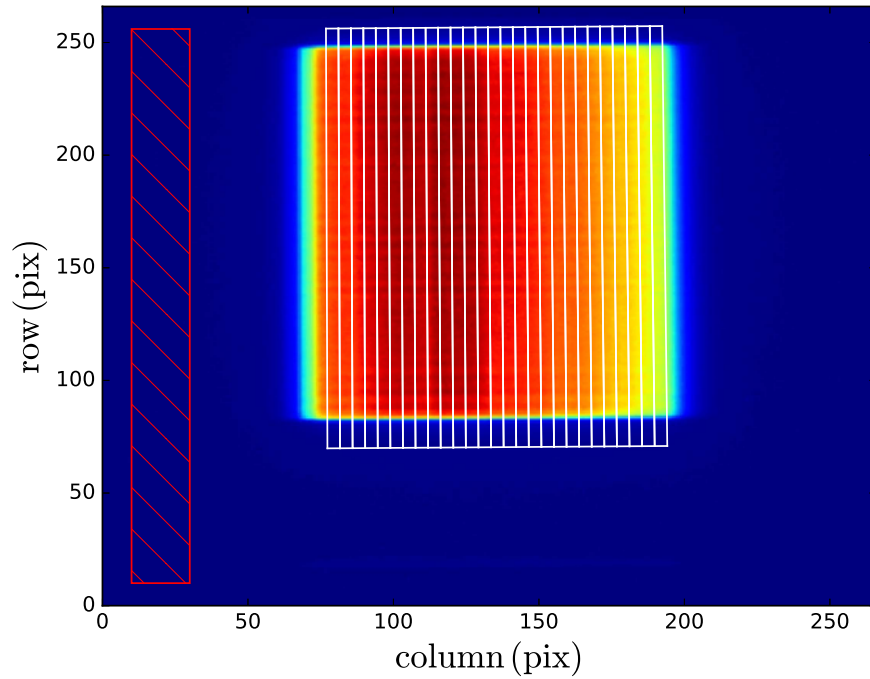
Figure 6. Photometric apertures for the different wavelength channels and the area (red square) from which the sky background ratio is estimated.
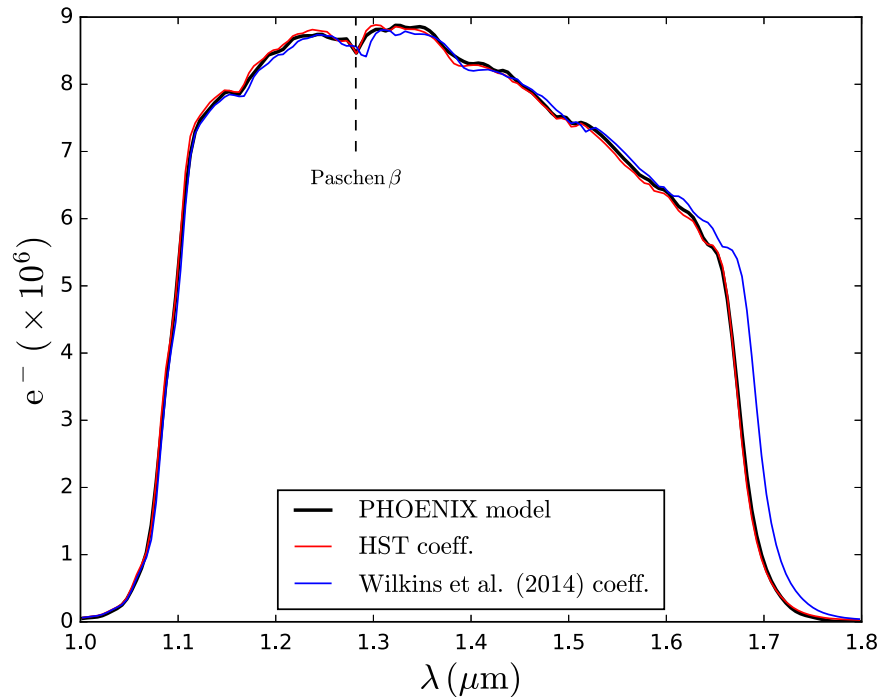

Figure 7. Extracted 1D spectrum using our method with the *HST* calibration coefficients (red), and those proposed by Wilkins et al. (2014) (blue). For comparison, the PHOENIX model of the host star scaled by sensitivity curve of the G141 grism (black), and the position of the Paschen β line.

analytic integral of this function inside the common area of the pixel, which we want to split, and the extraction aperture.

Overall, by taking into account simultaneously the geometrical distortions (dispersion variations across the scanning direction and inclined spectrum) and the positional shifts (horizontal and vertical), our calibration and extraction pipeline has two main advantages:

1. the photometric apertures are consistent with the geometric structure of the spatially scanned spectra across the detector, improving the consistency between

short and long scans threefold, compared to summing along the columns (Figure 8),

2. the extracted 1D spectra are consistent with the sensitivity curve of the G141 grism (Figure 7), suggesting that there is no need to change the *HST* calibration coefficients (used in Equations (4) and (5)), as proposed by Wilkins et al. (2014).

We will make the complete results for reduction, calibration and extraction, available to the community in the near future. Meanwhile, all our intermediate results (reduced data and light
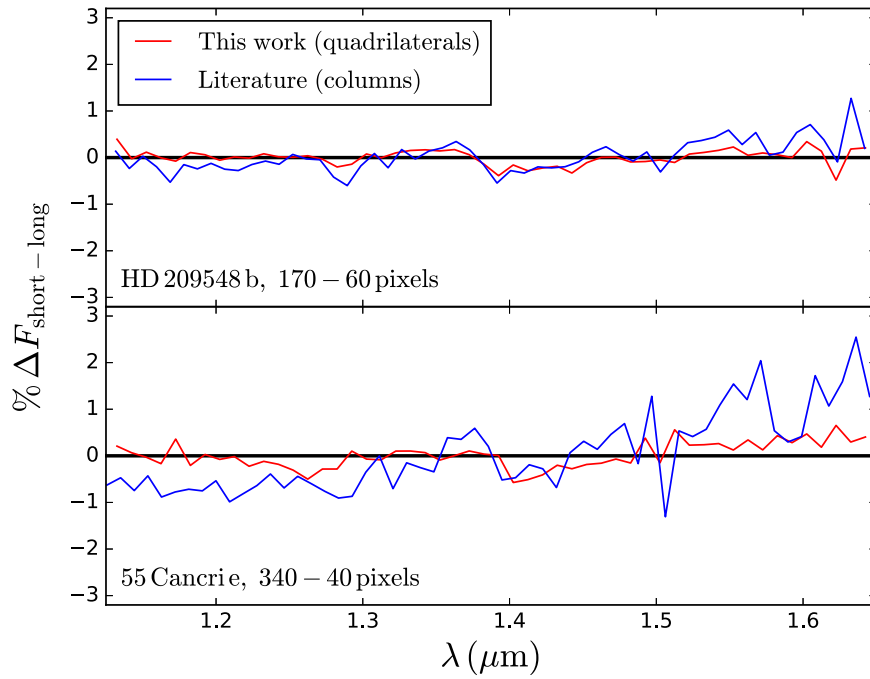
8

Figure 8. Percentage difference between the flux rate extracted from a short, intermediate scan and the long, final scan of the same exposure, using our method (red) and the sum along the columns (blue). At the top, the case of HD 209458 b, studied in this work, and at the bottom, the case of 55 Cancri e (Tsiaras et al. 2016), a much longer scan. In both cases, our method gives threefold better rms.
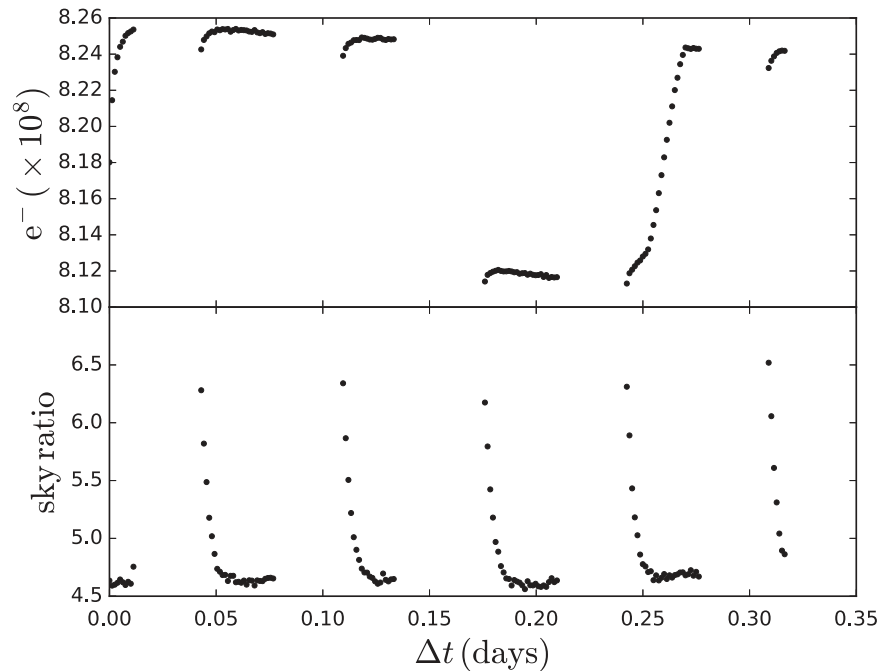

Figure 9. Raw white light curve and sky background relative to the master-sky frame.

curves) are available for direct comparisons with other methods.[8]

3. LIGHT CURVE ANALYSIS

3.1. Fitting the White Light Curve

Having extracted the 1D spectra from all the frames, we produce the white and spectral light curves. It is known from previous studies of observations with WFC3 in staring-mode (Berta et al. 2012; Swain et al. 2013; Wilkins et al. 2014) and scanning mode (Deming et al. 2013; Knutson et al. 2014a; Kreidberg et al. 2014b) that the infrared detector introduces two time-dependent systematics to the light curves of bright sources like HD 209458: one long-term (throughout the visit) with an approximately linear behavior and one short-term (throughout each *HST* orbit) with an approximately exponential behavior. These systematics are commonly referred to as the "ramps," and can be easily seen in the raw white light curve (Figure 9),

---

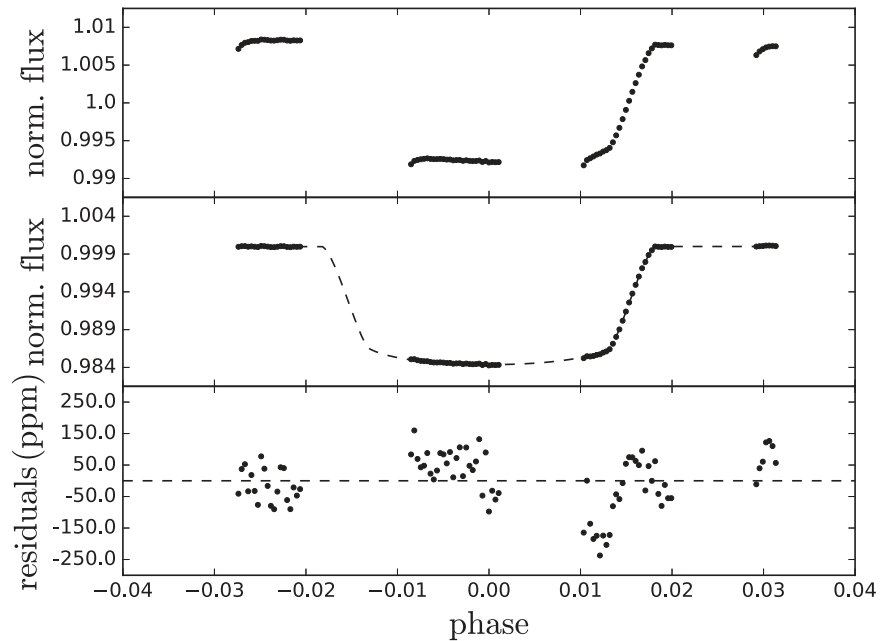[8] http://zuserver2.star.ucl.ac.uk/~atsiaras/wfc3/

Figure 10. Top: normalized raw white light curve. Middle: white light curve divided by the best-fit model for the systematics. Bottom: fitting residuals, where it can be seen that the model fails to fit the egress. The possible reasons for this behavior are either nonoptimal orbital parameters, limb-darkening coefficients or remaining systematics.

Table 2
White Light Curve Fitting Results

Limb-darkening Coefficients (1.125–1.650 μm)	
a_1	0.608377
a_2	-0.206186
a_3	0.262367
a_4	-0.133129
Fitted Transit Parameters	
T_0 (HJD)	$2456196.28836 \pm 0.00005$
R_p/R_*	0.12079 ± 0.00014

but are also present in the light curves of all wavelength channels. In this data set, the long-term ramp can be approximated by a linear function only after the third orbit. We do not include the first two orbits in our analysis, as a wrong fitting of the behavior of the instrument would introduce uncertainties to the final values of the transit parameters.

To correct these systematics, we fit a transit model, $F(t)$, multiplied by a normalization factor, n_w, and an instrumental systematics function, $R(t)$, (Kreidberg et al. 2014a, 2014b, 2015; Stevenson et al. 2014):

$$R(t) = (1 - r_a(t - T_0))(1 - r_{b1}e^{-r_{b2}(t - t_\mathrm{o})}) \qquad (10)$$

where t is time, T_0 is the mid-transit time, t_o is the time when each orbit starts, r_a is the slope of the linear, long-term "ramp" and (r_{b1}, r_{b2}) are the coefficients of the exponential short-term "ramp."

For the transit part of the light curve, we use our numerical model, which is written entirely in Python.[9] It returns the relative flux, $F(t)$, as a function of the limb-darkening coefficients, a_n, the R_p/R_* ratio and all the orbital parameters

(T_0, P, i, a/R_*, e, ω), based on the nonlinear limb-darkening model (Claret 2000) for the host star:

$$I(a_n, r) = 1 - \sum_{n=1}^{n=4} a_n(1 - (1 - r^2)^{n/4}). \qquad (11)$$

We calculate the limb-darkening coefficients by fitting an ATLAS model (Kurucz 1970; Howarth 2011; Espinoza & Jordán 2015). The ATLAS model is created using the stellar parameters in Table 1 and the sensitivity curve of the G141 grism, between 1.125 and 1.65 μm (Table 2). We use a circular orbit and fix the inclination and a/R_* ratio to the values of Table 1. Preselecting the values for the limb-darkening coefficients and the orbital parameters is necessary, as the asymmetry in the light curve (Figure 9) does not allow us to constrain them from the data.

As can be seen in the bottom panel of Figure 10, the residuals do not follow a Gaussian distribution at the transit egress. This behavior could be due to either nonoptimal values used for the inclination and a/R_* ratio or remaining systematics. For this reason, we rescale the uncertainties of the data points to the rms of the residuals and fit the light curve again. This increases the initial uncertainties approximately threefold. The fitting results and the final uncertainties can be found in Table 2. To verify the resulting spectrum and also reduce the uncertainties down to the noise floor and the residual error limit, a second measurement of the spectrum, time shifted to complete the phase coverage, would be required.

The correlations between the fitted parameters are shown in Figure 11. We find no correlation between the R_p/R_* ratio and any of the "ramp" parameters, while n_w, r_a and T_0 are correlated with each other. These correlations are introduced by the asymmetry in the light curve, as there is no constraint for the time of ingress. We do not find such correlations in the case of simulated symmetric light curves.
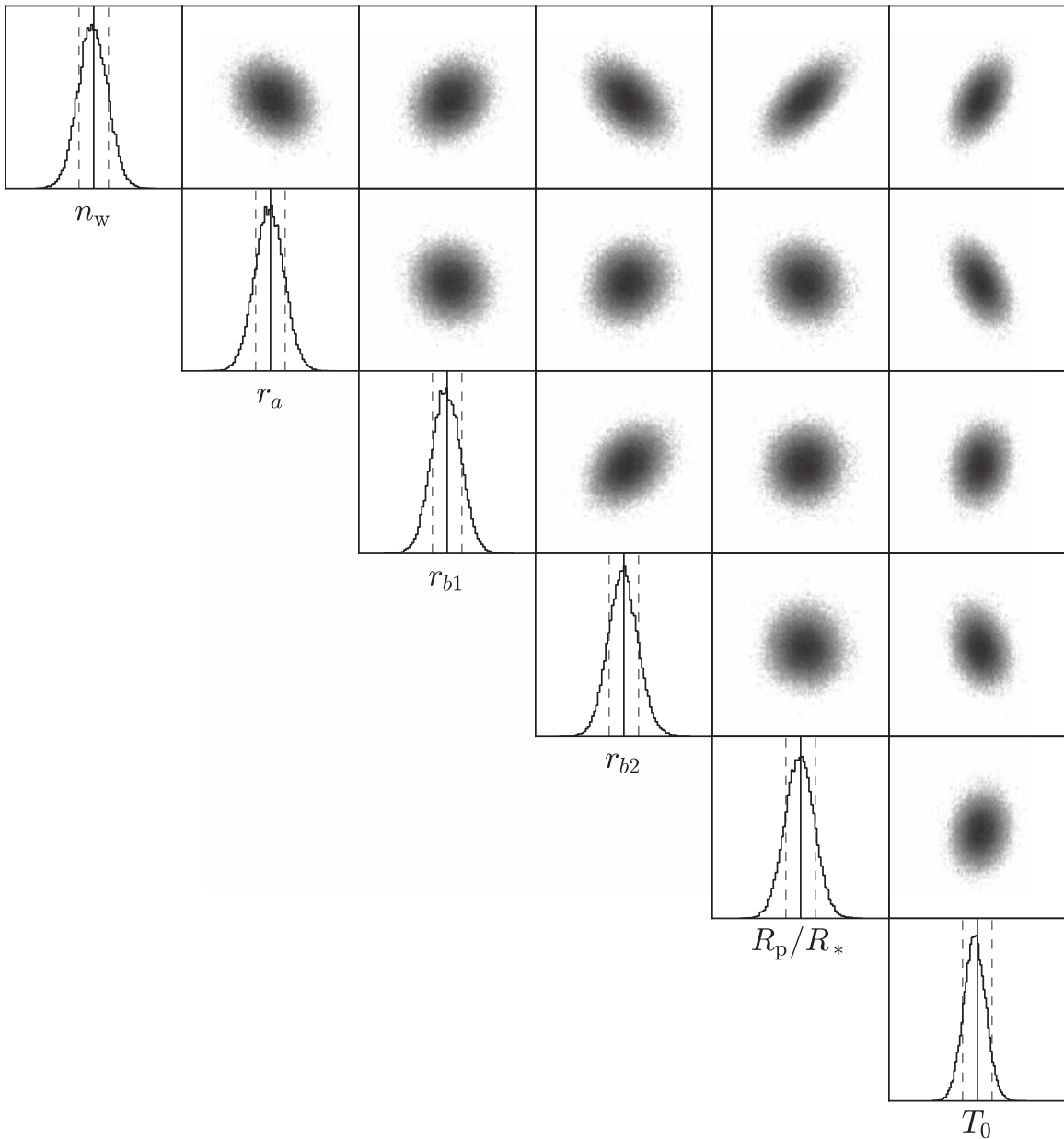
---

[9] https://github.com/ucl-exoplanets/pylightcurve

Figure 11. Correlations between the fitted systematics and transit parameters for the simultaneous fitting approach on all the data points. Apart from the expected correlation with the normalization factor, the R_p/R_* ratio is not correlated with any of the three parameters, which describe the systematics. In contrast, n_w, r_a and T_0 are correlated with each other, due to the asymmetric distribution of the data points around T_0.

3.2. Fitting the Spectral Light Curves

The wavelength bins are selected in such a way that: (a) the total flux is equally distributed among the bins, to have an approximately uniform S/N and (b) we avoid splitting the spectrum at wavelengths where the stellar spectrum has significant variations (1.165, 1.282, 1.372, and 1.502 μm). We calculate the limb-darkening coefficients for each spectral light curve using the ATLAS model, the stellar parameters in Table 1 and the sensitivity curve of the G141 grism inside the boundaries of each wavelength bin.

To extract the planetary spectrum from the spectral light curves, we follow two approaches similar to those described in Kreidberg et al. (2014b): (a) we fit each spectral light curve in the same way as the white one—i.e., fitting a wavelength-

dependent normalization factor, n_λ, a wavelength-dependent instrumental systematics function, $R(\lambda, t)$, and a wavelength-dependent transit model, $F(\lambda, t)$—(method 1) and (b) we divide each spectral light curve by the white one and then fit for a wavelength-dependent normalization factor, n_λ, a wavelength-dependent linear slope, linear with time, $1 + \chi_\lambda(t - T_0)$, and a wavelength-dependent relative transit model, $F(\lambda, t)/F_w(t)$, (method 2):

$$\text{method 1:} \qquad n_\lambda R(\lambda, t) F(\lambda, t)$$
$$\text{method 2:} \quad n_\lambda(1 + \chi_\lambda(t - T_0))(F(\lambda, t)/F_w(t)) \qquad (12)$$

where t is time, T_0 is the mid-transit time from Table 2, χ_λ is the coefficient of the wavelength-dependent linear slope, and $F_w(t)$ is the best-fit model on the white light curve (Section 3.1).
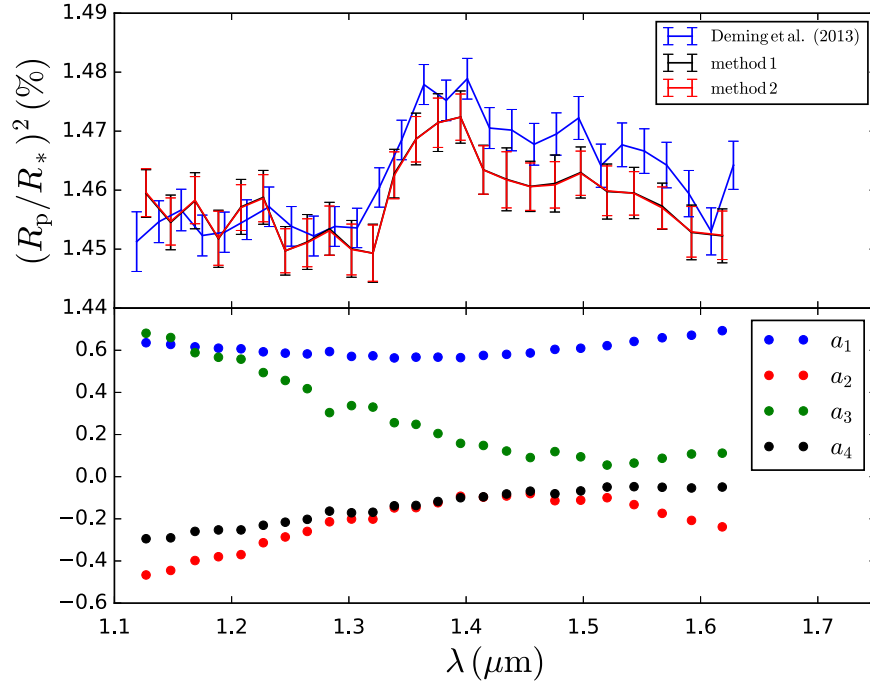
Figure 12. Top: comparison between the extracted spectra using the two different methods, and the spectrum from Deming et al. (2013). Bottom: limb-darkening coefficients (a_{1-4}) as functions of wavelength.

Table 3
Limb-darkening Coefficients a_{1-4} and Transit Depth for the Different Wavelength Channels

$\lambda_1-\lambda_2$ (μm)		a_1	a_2	a_3	a_4	$(R_p/R_*)^2$ ppm
1.1165	1.1375	0.635743	−0.466435	0.680708	−0.294517	14596 ± 41
1.1375	1.1585	0.627663	−0.444932	0.660394	−0.290206	14547 ± 40
1.1585	1.1790	0.616173	−0.397988	0.58849	−0.25968	14583 ± 40
1.1790	1.1985	0.609875	−0.379926	0.566774	−0.252676	14518 ± 46
1.1985	1.2175	0.606905	−0.369955	0.557771	−0.252625	14570 ± 39
1.2175	1.2365	0.592654	−0.313497	0.494043	−0.230553	14586 ± 40
1.2365	1.2550	0.586298	−0.286056	0.456591	−0.216029	14497 ± 37
1.2550	1.2740	0.582601	−0.259779	0.417679	−0.202415	14511 ± 41
1.2740	1.2930	0.593752	−0.214099	0.304066	−0.163396	14531 ± 42
1.2930	1.3115	0.570891	−0.201033	0.337262	−0.17122	14499 ± 43
1.3115	1.3295	0.573679	−0.201341	0.330334	−0.168801	14493 ± 48
1.3295	1.3480	0.563602	−0.148149	0.256247	−0.138194	14625 ± 40
1.3480	1.3665	0.567258	−0.146917	0.248296	−0.136497	14686 ± 38
1.3665	1.3855	0.567304	−0.123792	0.204782	−0.117829	14714 ± 42
1.3855	1.4050	0.565076	−0.0927791	0.158153	−0.0998947	14724 ± 39
1.4050	1.4245	0.575439	−0.0971152	0.148165	−0.0955357	14634 ± 41
1.4245	1.4445	0.580506	−0.0916465	0.121781	−0.0819971	14618 ± 48
1.4445	1.4650	0.587064	−0.0803535	0.0907723	−0.0687593	14606 ± 40
1.4650	1.4865	0.604201	−0.113934	0.119031	−0.0810911	14609 ± 39
1.4865	1.5090	0.609562	−0.111526	0.0943074	−0.0675727	14629 ± 37
1.5090	1.5315	0.62174	−0.0998157	0.0551344	−0.0490792	14599 ± 42
1.5315	1.5550	0.641863	−0.132576	0.0645796	−0.0474349	14595 ± 37
1.5550	1.5795	0.659312	−0.174048	0.0873337	−0.0501129	14570 ± 35
1.5795	1.6050	0.671289	−0.207513	0.107652	−0.0535945	14529 ± 43
1.6050	1.6320	0.692984	−0.238165	0.111607	−0.0491783	14524 ± 41

In all the $F(\lambda, t)$ models, the only free parameter is the R_p/R_* ratio, while the other parameters are the same as in the white light curve. We rescale the uncertainties of the data points to the rms of the residuals and fit again, in the same way as for the white light curve.

4. ATMOSPHERIC RETRIEVAL

We used the nested sampling algorithm implemented in $\mathcal{T}$-REx (Waldmann et al. 2015a, 2015b) to fully explore the parameter space and find the best fit to the WFC3 spectrum. Because of the limited number of data points in the observed
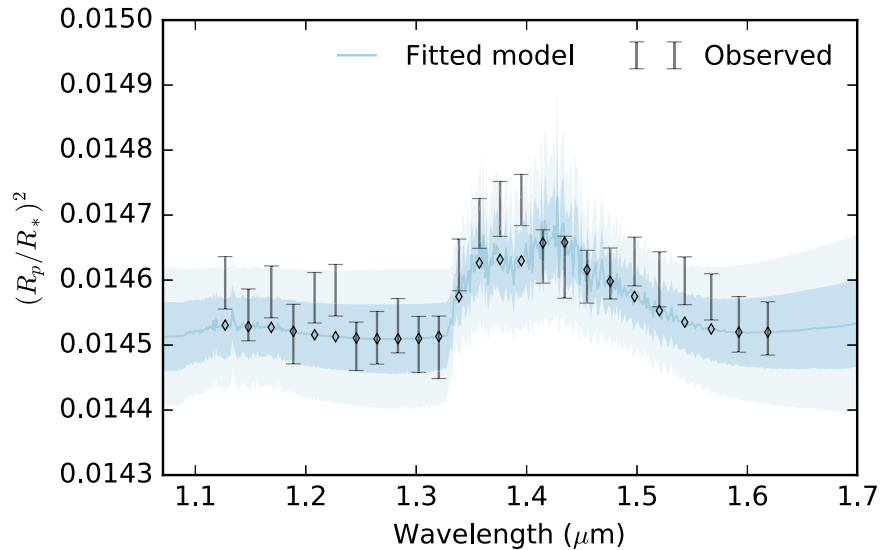
Figure 13. IR transmission spectrum of HD 209458 b (black error bars), with the best fit obtained with the second retrieval containing H_2O and clouds (blue line). The shaded regions show the the 1 and 2σ confidence intervals in the the retrieved spectrum.

spectrum, in order to significantly reduce the parameter space, we parameterize the atmosphere assuming an isothermal profile, with constant molecular abundances as a function of altitude. The fitted parameters are the temperature, the molecular abundances for the different species, the mean molecular weight, the radius at 10 bar, and the cloud top pressure—i.e., the pressure at which the cloud starts to be opaque. The cloud model used assumes an opaque and uniformly distributed cloud deck defined at a given pressure beyond which electromagnetic radiation is blocked at all wavelengths. We consider a broad range of absorbing molecules, including H_2O, HCN, NH_3, CH_4, CO_2, CO, NO, SiO, TiO, VO, H_2S, and C_2H_2.

We fit for the individual molecular abundances, assuming the bulk composition of the atmosphere to be made by a mixture of 85% hydrogen and 15% helium. We then couple the mean molecular weight to the atmospheric composition. We consider uniform priors for the molecular volume mixing ratios ranging between 10^{-12} and 10^{-2}. This prior is justified by the fact that in hot Jupiters the absolute abundances of absorbing gases are significantly smaller compared to the H_2O and He content. We also assume uniform priors for the temperature ($T = 1000–1800$ K), 10 bar radius ($R = 1.3–1.4\,R_{\rm Jup}$), and cloud top pressure ($P_{\rm cloud} = 10^{-5}–10^{-1}$ Pa). We run two retrievals, the first including 12 molecules and aimed at identifying the most likely trace gases, and the second including only the molecules identified in the first run, aimed at fully mapping the parameter space and at investigating the degeneracy of the model.

5. RESULTS

The limb-darkening coefficients, a_{1-4}, fitted on the ATLAS model, and the final measurements of the transit depth, $(R_{\rm p}/R_{*})^2$, as a function of wavelength, λ, are presented in Figure 12. The results from the two methods agree within 3 ppm, while the uncertainties are of the level of 40 ppm. However, the uncertainties in method 2 are improved by 10% compared to

method 1. Method 2 performs better because the "ramp" model, used in method 1, cannot reproduce perfectly the real systematics. We, therefore, use the results from method 2 (Table 3) in the spectral retrieval.

We found the slope of the long-term "ramp" to be wavelength-dependent, as well as the term χ_λ in model 2. This behavior supports the hypothesis that while the exponential "ramp" is a common mode between the white and the spectral light curve, the linear "ramp" is not, as seen in previous WFC3 observations (e.g., Deming et al. 2013; Fraine et al. 2014; Wilkins et al. 2014; Kreidberg et al. 2015).

Figure 12 also plots the spectrum obtained by Deming et al. (2013). While the two spectra include the same features, it can be seen that at longer wavelengths there is a systematic difference. This difference could be caused by the geometric distortions, which are stronger at longer wavelengths, or by the different way of taking into account the limb-darkening coefficients.

Figures 13 and 14 show the best fits to the spectrum obtained with $\mathcal{T}$-REx and the posterior distributions of the second spectral retrieval, respectively. The first retrieval including all molecules, shows that water is the strongest and most likely absorber, thus explaining the broad absorption feature at $\approx 1.35\,\mu$m. No other molecules seem to contribute to the overall spectrum, while clouds may be present to explain the flat spectrum seen between 1.1 and 1.3 μm. These results are in agreement with the previous analysis of this data set (Deming et al. 2013).

We, therefore, run the second retrieval including only H_2O and clouds. Figure 13 shows the best fit to the data corresponding to the maximum a posteriori solution of this Bayesian retrieval, while Figure 14 shows the posterior distributions of this retrieval. We find that the retrieved absolute abundance of H_2O is $3 \times 10^{-6}–3 \times 10^{-4}$. However, the posterior distributions (Figure 14) shows that this parameter is highly degenerate with the cloud top pressure and the the 10 bar radius. It is, therefore, impossible with these data alone to constrain the absolute abundances of this absorber.
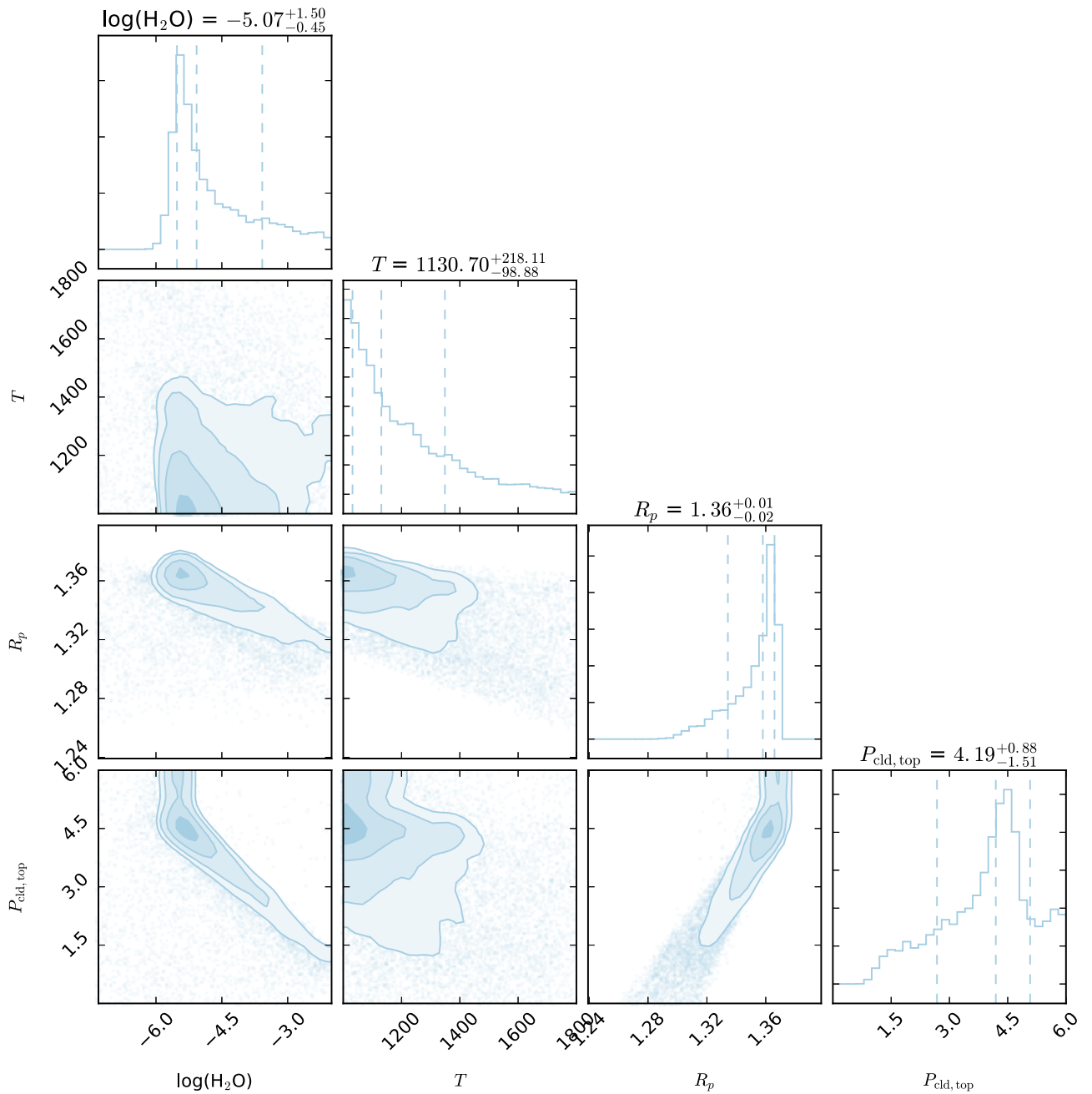
Figure 14. Posterior distributions of the second spectrum retrieval including H_2O and clouds.

We found the 10 bar radius to be $1.36^{+0.01}_{-0.02}$ $R_{\rm Jup}$. The posterior distributions also show that the data can be best explained by a cloud deck at 0.15 bar, but we note that the distribution is very broad (and degenerate with the other fitted parameters), and a solution without clouds or with lower-pressure clouds is also acceptable.

The first retrieval including all molecules has a global evidence $\log E = 209$, while the second retrieval including H_2O only has $\log E = 210$. Despite the global evidence of the H_2O-only retrieval being only marginally higher than that of the more complete model, this result shows that there is no statistical evidence that favors the presence of additional molecules in the spectrum.

Finally, we find the atmospheric mean temperature peaking toward the lower edge of the prior. As the prior bounds are justified by the equilibrium temperature of the planet and a reasonable range of possible albedos, this result shows that the current model likely biases the retrieved temperature toward lower values.

6. DISCUSSION AND CONCLUSIONS

The spatial scanning technique has improved the efficiency of the WFC3 camera compared to the staring-mode observations, as it allows longer exposure times for bright targets, minimizing the risk of saturating the sensitive detector.

Table 4
Lengths of the Different Subarrays

Array	L (pix)	Array	L (pix)
FULL	1024	SUB128	128
SUB512	512	SUB64	64
SUB256	256		

Table 5
Offsets from the F140W Filter

Filter	x_{off} (pix)	Filter	x_{off} (pix)
F098W	0.150	F132N	0.039
F140W	0.083	F126N	0.264
F153M	0.146	F167N	0.196
F139M	0.110	F164N	0.169
F127M	0.131	F160W	0.136
F128N	0.026	F125W	0.064
F130N	0.033	F110W	−0.073

Table 6
Chip Reference Pixels and Pixel Scales for the Different WFC3 Apertures (IR Channel)

WFC3 Aperture	x_{ref} (pix)	x_{scale} ("/pix)
IR	562.0	0.135601
IR—G102 and G141	497.0	0.135603
IRSUB64/128/256/512	522.0	0.135470
GRISM1024—G102 and G141	497.0	0.135603
GRISM1024	497.0	0.135603
GRISM512—G102 and G141	505.0	0.135504
GRISM512	505.0	0.135504
GRISM256—G102 and G141	410.0	0.135508
GRISM256	410.0	0.135508
GRISM128/64—G102	376.0	0.135476
GRISM128/64—G141	410.0	0.135474
GRISM128/64	496.0	0.135404

However, unlikely staring spectra, spatially scanned spectra are affected by the field-dependent characteristics of the G141 grism (dispersion variations across the scanning direction and inclined spectrum). In addition, scanning-mode observations include positional shifts (horizontal and vertical), which are an order of magnitude stronger than staring-mode observations.

We developed a new pipeline designed to minimize these effects on the spatially scanned spectra, by including alternative calibration and extraction techniques and using a coordinate system along the wavelength/scanning axes instead of the x/y axes of the detector. We found discrepancies up to 1% the flux of the star between scans, which differ by 100 pixels in length. Consequently, for scan lengths of this range and beyond, the geometric distortions should be taken into account. We also found that the effect becomes stronger as the scan length increases. Our approach ensures the more efficient analysis of scans longer than 100 pixels, and, therefore, of longer exposure times for bright targets, as demonstrated in Tsiaras et al. (2016).

As a test case, we reanalyzed the spatially scanned spectra during the transit of HD 209458 b. Because of the incomplete phase coverage, we were not able to investigate in more detail the effect of the time-dependent systematics on this data set. To further calibrate and verify the repeatability of the results obtained, a second, time-shifted observation would be necessary.

The interpretation of the final spectrum with our retrieval code $\mathcal{T}$-REx, confirms the presence of water vapor and also suggests the presence of clouds, in agreement with the literature. However, we note that it is not possible to determine the absolute abundances of this gas. To address this issue, additional infrared spectroscopic observations, over a broader wavelength range, are needed.

APPENDIX A
TARGET POSITION

During the calibration process, as explained in Section 2.4, we calculate the physical position of the star on the detector using Equation (2):

$$x^* = x_0 + (507 - 0.5L) + \Delta x_{off} + \Delta x_{ref}.$$

Here, we give the values of all the parameters used in this calculation for all different subarrays, filters and apertures, apart from x_0, which is the result of fitting a 2D Gaussian function to the direct image.

L is the size of the direct image (Table 4) and the correction 507–0.5L is needed to transform the calculated x-position from the coordinate system of the subarray used for the direct image to that of the full detector array. It is a result of the fact that all the subarrays have the same center as the full detector array. We also have to mention that the calibration coefficients do not take into account the reference pixels and so the center is 507 instead of 512.

Δx_{off} is the difference in the centroid offsets along the x-axis between the filter used for the direct image and the F140W filter, as calculated by Sabbi et al. (2010) (Table 5). This correction is needed, because all the calibration coefficients have been calculated relative to direct images with the F140W filter.

Finally, Δx_{ref} is the difference in the chip reference pixels between the WFC3 aperture used for the direct image and the aperture used for the dispersed image (Table 6). The reference pixel is the pixel where the given target coordinates are fixed by the telescope. It is usual to have a shift between the other filters and the two grisms, in order for the spectrum to fit inside the subarray. This correction also includes any shifts indicated by the observer through the POSTARG1 keyword in the fits file header (converted to pixels). Table 6 contains most of the available apertures, while a complete list can be found on the STScI website.[10]

APPENDIX B
WAVELENGTH GRID EQUATIONS

In Section 2.4, we use Equation (6) to calculate the position of the incoming photons (x_λ, y_λ) as a function of wavelength (λ) for a given physical position of the star on the full detector

---

[10] http://www.stsci.edu/hst/observatory/apertures/wfc3.html

Table 7
Trace and Wavelength Solution Calibration Coefficients for the G141 Grism (Kuntschner et al. 2009)

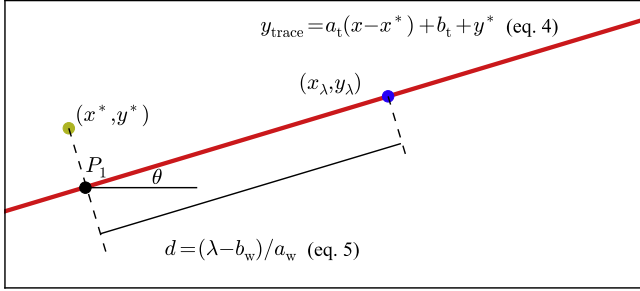|	$n = 0$	$n = 1$ [x^*]	$n = 2$ [y^*]	$n = 3$ [$x^* y^*$]	$n = 4$ [x^{*2}]	$n = 5$ [y^{*2}]
a_{tn}	1.04275E–02	−7.96978E–06	−2.49607E–06	1.45963E–09	1.39757E–08	4.8494E–10
b_{tn}	1.96882E+00	9.09159E–05	−1.93260E–03	$\cdots$	$\cdots$	$\cdots$
a_{wn}	4.51423E+01	3.17239E–04	2.17055E–03	−7.42504E–07	3.48639E–07	3.09213E–07
b_{wn}	8.95431E+03	9.35925E–02	$\cdots$	$\cdots$	$\cdots$	$\cdots$

Figure 15. Relative positions of the trace (red line), the direct image of the star (x^*, y^*), and a random point on the trace (x_λ, y_λ).

array (x^*, y^*):

$$x_\lambda = x^* - \frac{b_t a_t}{a_t^2 + 1} + \frac{\lambda - b_w}{a_w} \cos[\tan^{-1}(a_t)]$$

$$y_\lambda = a_t(x_\lambda - x^*) + b_t + y^*$$

where $(a_{tn}, b_{tn}, a_{wn}, b_{wn})$ are the calibration coefficients, which are also functions of x^* and y^*, as defined in Equations (4) and (5) (see also Table 7).

We derive them based on Equations (4) and (5), and Figure 15, which shows the position of the star, $P^*(x^*, y^*)$, and the photons of a particular wavelength, $P_\lambda(x_\lambda, y_\lambda)$, with respect to the spectrum trace (red line). Let $P_1(x_1, y_1)$ be the projection of P^* on the trace. Because P_1 is on the trace, from Equation (4) we have:

$$y_1 - y^* = a_t(x_1 - x^*) + b_t. \tag{13}$$

Since P_1 is the projection of P^* on the trace, the vectors $P^* P_1 = (x_1 - x^*, y_1 - y^*)$ and $V = (1, a_t)$ (vector parallel to the trace) are orthogonal, so:

$$P^* P_1 \cdot V = 0 \Rightarrow x_1 - x^* + a_t(y_1 - y^*) = 0 \overset{(13)}{\Rightarrow}$$
$$x_1 - x^* + a_t(a_t(x_1 - x^*) + b_t)$$
$$= 0 \Rightarrow (x_1 - x^*)(1 + a_t^2) + a_t b_t = 0 \Rightarrow$$
$$x_1 = x^* - \frac{a_t b_t}{1 + a_t^2}. \tag{14}$$

Also, from Equation (5), the distance between P_1 and P_λ along the spectrum trace is:

$$d = \frac{\lambda - b_w}{a_w}. \tag{15}$$

Finally, let θ be the inclination of the trace ($\theta = \tan^{-1}(a_t)$) with respect to the x-axis of the detector:

$$\cos(\theta) = \frac{x_\lambda - x_1}{d} \Rightarrow x_\lambda = x_1 + d \cos[\tan^{-1}(a_t)] \overset{(14), (15)}{\Rightarrow}$$

$$x_\lambda = x^* - \frac{a_t b_t}{1 + a_t^2}$$
$$+ \frac{\lambda - b_w}{a_w} \cos[\tan^{-1}(a_t)].$$

P_λ is also on the trace, and so, from Equation (4):

$$y_\lambda = a_t(x_\lambda - x^*) + b_t + y^*.$$

REFERENCES

Barman, T. 2007, ApJL, 661, L191
Beaulieu, J. P., Kipping, D. M., Batista, V., et al. 2010, MNRAS, 409, 963
Ben-Jaffel, L., & Sona Hosseini, S. 2010, ApJ, 709, 1284
Berta, Z. K., Charbonneau, D., Désert, J.-M., et al. 2012, ApJ, 747, 35
Burrows, A., Hubeny, I., Budaj, J., Knutson, H. A., & Charbonneau, D. 2007, ApJL, 668, L171
Charbonneau, D., Brown, T. M., Latham, D. W., & Mayor, M. 2000, ApJL, 529, L45
Charbonneau, D., Brown, T. M., Noyes, R. W., & Gilliland, R. L. 2002, ApJ, 568, 377
Claret, A. 2000, A&A, 363, 1081
Crouzet, N., McCullough, P. R., Burke, C., & Long, D. 2012, ApJ, 761, 7
Crouzet, N., McCullough, P. R., Deming, D., & Madhusudhan, N. 2014, ApJ, 795, 166
Cutri, R. M., Skrutskie, M. F., van Dyk, S., et al. 2003, yCat, 2246
Danielski, C., Deroo, P., Waldmann, I. P., et al. 2014, ApJ, 785, 35
Deming, D., Seager, S., Richardson, L. J., & Harrington, J. 2005, Natur, 434, 740
Deming, D., Wilkins, A., McCullough, P., et al. 2013, ApJ, 774, 95
Dressel, L. 2012, Wide Field Camera 3 Instrument Handbook for Cycle 21 v. 5.0 (Baltimore, MD: STScI)
Dulude, M. J., Baggett, S., & Hilbert, B. 2014, New WFC3/IR Dark Calibration Files, Tech. rep. (Baltimore, MD: STScI)
Espinoza, N., & Jordán, A. 2015, MNRAS, 450, 1879
Evans, T. M., Aigrain, S., Gibson, N., et al. 2015, MNRAS, 451, 680
Fraine, J., Deming, D., Benneke, B., et al. 2014, Natur, 513, 526
Griffith, C. A. 2014, RSPTA, 372, 30086
Hilbert, B. 2012, WFC3/IR Cycle 19 Bad Pixel Table Update, Tech. rep. (Baltimore, MD: STScI), http://adsabs.harvard.edu/abs/2012wfc.. rept...10H
Hilbert, B. 2014, Updated nonlinearity calibration method for WFC3/IR, Tech. rep. (Baltimore, MD: STScI), http://adsabs.harvard.edu/abs/2014wfc.. rept...17H
Hollis, M. D. J., Tessenyi, M., & Tinetti, G. 2013, CoPhC, 184, 2351
Holmström, M., Ekenbäck, A., Selsis, F., et al. 2008, Natur, 451, 970
Howarth, I. D. 2011, MNRAS, 413, 1515
Knutson, H. A., Benneke, B., Deming, D., & Homeier, D. 2014a, Natur, 505, 66
Knutson, H. A., Charbonneau, D., Allen, L. E., Burrows, A., & Megeath, S. T. 2008, ApJ, 673, 526
Knutson, H. A., Charbonneau, D., Noyes, R. W., Brown, T. M., & Gilliland, R. L. 2007, ApJ, 655, 564

Knutson, H. A., Dragomir, D., Kreidberg, L., et al. 2014b, ApJ, 794, 155
Kreidberg, L., Bean, J. L., Désert, J.-M., et al. 2014a, ApJL, 793, L27
Kreidberg, L., Bean, J. L., Désert, J.-M., et al. 2014b, Natur, 505, 69
Kreidberg, L., Line, M. R., Bean, J. L., et al. 2015, arXiv:1504.05586
Kümmel, M., Kuntschner, H., Walsh, J. R., & Bushouse, H. 2011, Master sky images for the WFC3 G102 and G141 grisms, Tech. rep., http://adsabs.harvard.edu/abs/2011wfc..rept....1K
Kuntschner, H., Bushouse, H., Kümmel, M., & Walsh, J. R. 2009, WFC3 SMOV proposal 11552: Calibration of the G141 grism, Tech. rep., http://adsabs.harvard.edu/abs/2009wfc..rept...17K
Kuntschner, H., Kümmel, M., Walsh, J. R., & Bushouse, H. 2011, Revised Flux Calibration of the WFC3 G102 and G141 grisms, Tech. rep, http://adsabs.harvard.edu/abs/2011wfc..rept....5K
Kurucz, R. L. 1970, SAO Special Report, 309
Line, M. R., Knutson, H., Wolf, A. S., & Yung, Y. L. 2014, ApJ, 783, 70
Line, M. R., Stevenson, K. B., Bean, J., et al. 2016, arXiv:1605.08810
Linsky, J. L., Yang, H., France, K., et al. 2010, ApJ, 717, 1291
Madhusudhan, N., & Seager, S. 2009, ApJ, 707, 24
Majeau, C., Agol, E., & Cowan, N. B. 2012, ApJL, 747, L20
McCullough, P. R., Crouzet, N., Deming, D., & Madhusudhan, N. 2014, ApJ, 791, 55
Rajan, A. (ed.) 2011, WFC3 Data Handbook v. 2.1 (Baltimore, MD: STScI)
Redfield, S., Endl, M., Cochran, W. D., & Koesterke, L. 2008, ApJL, 673, L87
Rothman, L. S., Gordon, I. E., Babikov, Y., et al. 2013, JQSRT, 130, 4
Rothman, L. S., Gordon, I. E., Barbe, A., et al. 2009, JQSRT, 110, 533
Rothman, L. S., Gordon, I. E., Barber, R. J., et al. 2010, JQSRT, 111, 2139
Sabbi, E., MacKenty, J., & Borders, T. 2010, Proposal 11913-IR Filter Wedge Check, Tech. rep., http://adsabs.harvard.edu/abs/2010ifc..rept...12S

Schwarz, H., Brogi, M., de Kok, R., Birkby, J., & Snellen, I. 2015, A&A, 576, A111
Sing, D. K., Fortney, J. J., Nikolov, N., et al. 2016, Natur, 529, 59
Sing, D. K., Vidal-Madjar, A., Désert, J.-M., Lecavelier des Etangs, A., & Ballester, G. 2008, ApJ, 686, 658
Snellen, I. A. G., Albrecht, S., de Mooij, E. J. W., & Le Poole, R. S. 2008, A&A, 487, 357
Snellen, I. A. G., Brandl, B. R., de Kok, R. J., et al. 2014, Natur, 509, 63
Snellen, I. A. G., de Kok, R. J., de Mooij, E. J. W., & Albrecht, S. 2010, Natur, 465, 1049
Stevenson, K. B., Désert, J.-M., Line, M. R., et al. 2014, Sci, 346, 838
Swain, M., Deroo, P., Tinetti, G., et al. 2013, Icar, 225, 432
Swain, M. R., Deroo, P., Griffith, C. A., et al. 2010, Natur, 463, 637
Swain, M. R., Tinetti, G., Vasisht, G., et al. 2009a, ApJ, 704, 1616
Swain, M. R., Vasisht, G., Tinetti, G., et al. 2009b, ApJL, 690, L114
Tinetti, G., Deroo, P., Swain, M. R., et al. 2010, ApJL, 712, L139
Todorov, K. O., Deming, D., Knutson, H. A., et al. 2013, ApJ, 770, 102
Torres, G., Winn, J. N., & Holman, M. J. 2008, ApJ, 677, 1324
Tsiaras, A., Rocchetto, M., Waldmann, I. P., et al. 2016, ApJ, 820, 99
Vidal-Madjar, A., Lecavelier des Etangs, A., Désert, J.-M., et al. 2003, Natur, 422, 143
Waldmann, I. P., Rocchetto, M., Tinetti, G., et al. 2015a, ApJ, 813, 13
Waldmann, I. P., Tinetti, G., Deroo, P., et al. 2013, ApJ, 766, 7
Waldmann, I. P., Tinetti, G., Drossart, P., et al. 2012, ApJ, 744, 35
Waldmann, I. P., Tinetti, G., Rocchetto, M., et al. 2015b, ApJ, 802, 107
Wilkins, A. N., Deming, D., Madhusudhan, N., et al. 2014, ApJ, 783, 113
Yurchenko, S. N., & Tennyson, J. 2014, MNRAS, 440, 1649
Zellem, R. T., Griffith, C. A., Deroo, P., Swain, M. R., & Waldmann, I. P. 2014, ApJ, 796, 48